Received: 14 April 2021 | Revised: 14 June 2021 | Accepted: 14 June 2021

DOI: 10.1002/cjce.24288

ARTICLE

THE CANADIAN JOURNAL OF CHEMICAL ENGINEERING

Modelling adsorption based on an isoreticular MOF-series of IFPs—Part II: Dynamic adsorption in fixed beds

Dirk Otter[1] | **Max Dieler**[1] | **Volker Dänekas**[1] | **Christian Geitner**[2] | **Lorenz Krätz**[1] | **Hans-Jürgen Holdt**[3] | **Hans-Jörg Bart**[1]

[1]Lehrstuhl für Thermische Verfahrenstechnik, Technische Universität Kaiserslautern, Kaiserslautern, Germany

[2]Bereichsorganisation Prozesse, Fraunhofer UMSICHT, Oberhausen, Germany

[3]Institut für Chemie, Anorganische Chemie, Universität Potsdam, Potsdam, Germany

Correspondence
Hans-Jörg Bart, Lehrstuhl für Thermische Verfahrenstechnik, Technische Universität Kaiserslautern, Gottlieb-Daimler-Straße 44, 67663 Kaiserslautern, Germany.
Email: bart@mv.uni-kl.de

Abstract

Based on experimental pure component data for the characterization of the isostructural imidazolate framework Potsdam (IFP) series reported in Part I, a model for the simulation of non-isothermal dynamic adsorption of CO_2/CH_4-mixtures in fixed-bed columns is presented in this Part II. The robustness of the model is examined and validated, by comparison to experimental breakthrough data at different process conditions, such as varying concentration, temperature, and pressure. Thereby, different predictive methods for the estimation of adsorption equilibria of mixtures are compared (RAST, IAST, ML). The results show that ideal behaviour can be assumed with good accuracy for the system under consideration, except for IFP-2, which shows significant deviations at increased pressures and temperatures. A detailed kinetic analysis reveals that mass transfer is significantly influenced by micropore diffusion. Thus, only for IFP-1 the dynamic separation of CO_2 and CH_4 is equilibrium-driven, while for the remaining IFPs the kinetic regime dominates the process, which in some cases increases the separation efficiency (IFP-2 to -7) but can also inhibit it (IFP-8). The determined intracrystalline diffusion coefficients show very good agreement with values for metal organic framework (MOF) compounds of similar structure reported in the literature.

KEYWORDS

adsorption kinetics, breakthrough experiments, dynamic adsorption, IAST/RAST, multicomponent adsorption equilibria

1 | INTRODUCTION

In 2019 the share of natural gas (NG) in the primary energy sector rose to a record high of 24.2%.[1] The increased global demand for natural gas has led to the utilization of reserves that were previously considered economically unviable. Next to other impurities like N_2 and H_2S, the CO_2 content of raw NG can vary significantly depending on the source location.[2] In addition, major efforts are being made to partially replace fossil fuels with biogas produced by anaerobic digestion of biological materials, which also contains significant amounts of CO_2 depending on the origin of the biological substrates and fermentation conditions.[3,4]

The presence of CO_2 not only reduces the calorific value, but can also cause sweet gas corrosion by

formation of carbonic acid in the presence of ubiquitous H_2O inside the pipelines.[5,6]

Therefore, the composition of gas delivered to commercial pipeline grids is strictly controlled and must meet certain specifications. The maximum CO_2 content in NG pipelines is usually set to 2%.[7] Processes suitable for carbon dioxide removal include physical absorption in water or organic solvents (pressure washing, Selexol process), reactive sorption in aqueous amine solvents (amine washing), multistage membrane separation processes or cryogenic condensation, and pressure swing adsorption (PSA).[8]

Numerical simulation of the dynamic separation of CH_4/CO_2-mixtures in adsorption columns requires comprehensive knowledge of the physicochemical properties of both the gas and solid phase. The transient transport phenomena involve the coupled exchange of mass and energy, described by balance equations. Adsorption equilibria and kinetics are the limiting key quantities in order to describe the mass transfer between the gas phase and the microporous adsorbent. The morphological properties as well as the experimental determination and modelling of pure component adsorption equilibria for CO_2 and CH_4 are reported for selected imidazolate framework Potsdam (IFP) species (IFP-1 to -8) in Part I of this study.[9] These results offer the possibility to simulate the dynamic and non-isothermal separation of CO_2/CH_4 mixtures under consideration of the heat of adsorption, which is also derived from the pure component data.[9]

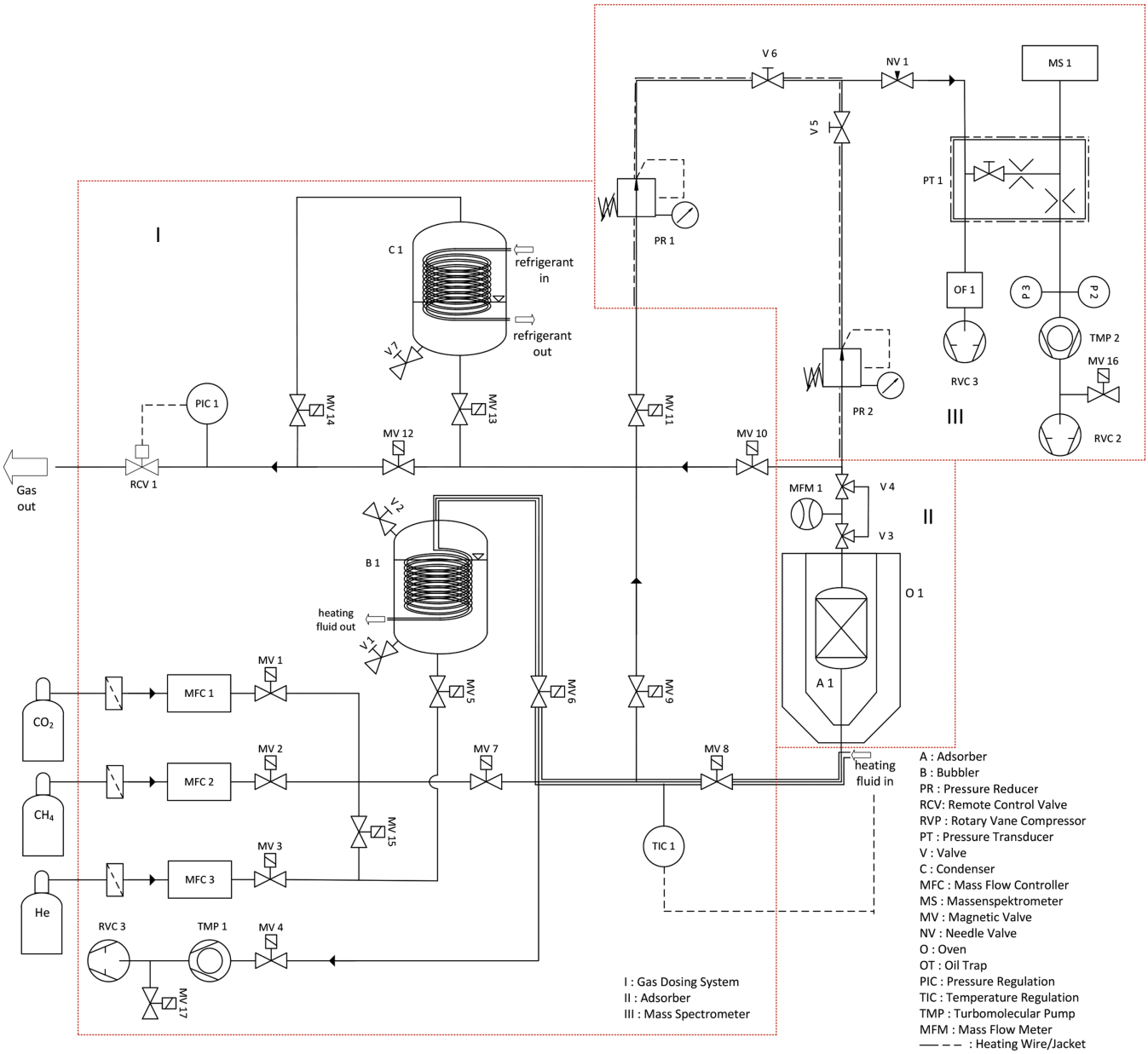

FIGURE 1 Flow chart of the experimental breakthrough plant consisting of the gas dosing system (I), the adsorber unit (II), and the gas analysis (III)

2 | MATERIAL AND METHODS

2.1 | Experimental setup

All breakthrough experiments are performed on a self-constructed test rig (see Figure 1), which can be categorized into three functional subsystems: the gas dosing system (I), the adsorber unit (II), and gas analysis (III). With the gas dosing system, ternary gas mixtures of different concentrations can be generated via three thermal mass flow controllers (MFC 1–3) and optionally humidified in a bubbler system (B 1). The overall flow rate for each experiment flowrate is set to 30 ml_{STP} min^{-1}. Before the gas phase composition is detected in real time in the gas analysis section (III) by a quadrupole mass spectrometer (MS 1), it can optionally be passed through or by the adsorption unit (II), which consists of an adsorber column (A 1) with a fixed bed volume of approximately 1 ml ($l_b = 50\,mm$, $d_b = 5\,mm$). Since the particle diameters of the used adsorbents are significantly below 500 µm, slip flows caused by wall effects, which can occur in packed beds if the bed to particle diameter ratio drops to values below 10,[10] can be excluded. The change in flow rate due to adsorption is recorded using a thermal mass flow meter (MFM 1). The system pressure is controlled downstream of the adsorber by a remotely controlled valve (RCV 1). Prior to each experiment, the system pressure is established with helium. To gain more insight into the influence of the plant periphery, such as pipes and fixtures, residence time distributions are determined with inert particles that do not interact with the gas phase and are of the same size distribution as the adsorbent. Via a mass balance by integration of the concentration profiles obtained in this way at the outlet of the adsorber over the time, the absolute adsorbed amount of each species, i, is inferred[11]:

$$n_{i,T,p}^{ads} = \frac{p}{R\,T}\int_{t_0}^{t_\infty}\left(\dot{V}_{in}(t)y_{i,in}(t) - \dot{V}_{out}(t)y_{i,out}(t)\right)dt \tag{1}$$

The numerical integration of the measurement data is performed using Euler's midpoint formula for the approximation of Riemann integrals[12]:

$$\int_a^b f(x)\,dx \approx \sum_{j=1}^{n}\left(x_{j+1}-x_j\right)\left(\frac{f\left(x_j\right)+f\left(x_{j+1}\right)}{2}\right) \tag{2}$$

The associated estimated error, which is proportional to the interval size, $[a,b]$, and indirectly proportional to the number of increments, n, is shown in Equation (3):

$$\left|\int_a^b f(x)\,dx - \sum_{j=1}^{n}\left(x_{j+1}-x_j\right)\right| \le \frac{(b-a)^3}{24\,n}\left\|f''(x)\right\|_\infty \tag{3}$$

2.2 | Modelling adsorption equilibria of mixtures

For the modelling of dynamic adsorption of mixtures, multicomponent equilibria must be known initially. Since they are difficult to determine experimentally, there are predictive approaches to estimate them a priori.

The most common method is the theory of the ideal adsorbed solution (IAST) developed by Myers and Prausnitz in 1965,[13] which, like the isosteric method,[9] relies on the thermodynamic equilibrium condition of the change in Gibbs free energy:

$$dg^g = s^g\,dT - v^g\,dp = dg^\pi = s^\pi\,dT - v^\pi\,dp + \sum_{i=1}^{n}\left.\frac{\partial g^\pi}{\partial n}\right|_{T,p} dn_i \tag{4}$$

This relation can be simplified to the Gibbs isotherm for constant temperature,[14] with the spreading pressure, π_i, the adsorbed amount, n_i, and the interface between the gas and adsorbate phase, A:

$$\frac{A}{n_i}\,d\pi_i + v_i^\pi\,dp_i = v_i^g\,dp_i \tag{5}$$

Applying the ideal gas law and assuming that the adsorbate volume is negligible compared to the volume of the gas phase yields Equation (6):

$$v_i^g = \frac{R\,T}{p_i} \gg v^\pi \tag{6}$$

Finally, the following physical dependency of the spreading pressure is obtained after insertion of Equation (6) in Equation (5) and subsequent rearrangement:

$$\frac{\pi_i A}{R\,T} = \int_0^{p_i^0} n_i(p_i)d\ln p_i \tag{7}$$

where p_i^0 denotes the pure components adsorbate vapour pressure for component i at the spreading pressure of the mixture and thus differs from the partial pressure in case of mixture adsorption. This deviation is described analogously to Raoult's law known for vapour-liquid equilibria:

$$p\,y_i = p_i^0(\pi)\,x_i\,\gamma_i \tag{8}$$

where p denotes the gas phase pressure and γ_i the activity coefficient, while y_i and x_i denote the molar fractions of the gas and liquid phase, respectively. From the equilibrium assumption of the adsorbate phase, the condition follows that the spreading pressures must be equal for all components i. After coupling of Equations (7) and (8) via p_i^0, an adsorbate phase composition can be clearly assigned to each gas phase composition by iterative solution.

The total amount adsorbed, n_t, corresponds to the single component loading at given partial pressure, $n_i(p_i)$, according to the Gibbs-Duhem relation[15]:

$$\frac{1}{n_t} = \sum_{i=1}^{n} \frac{x_i}{n_i(p_i)} + \sum_{i=1}^{n} x_i \left(\frac{\partial ln\,\gamma_i}{\partial \frac{\pi A}{RT}} \right)_{T, x_j \neq x_i} \tag{9}$$

Finally, the load contributions of the components involved in the adsorbed solution can be determined in analogy to Dalton's law for the gas phase:

$$n_i = x_i\,n_t \tag{10}$$

Assuming an ideal system, the activity coefficient can be set equal to unity, simplifying Equations (8) and (9) accordingly. Based on the IAST, the multi-Langmuir (ML) equation according to Markham and Benton[16] can also be derived, which is theoretically only thermodynamically consistent if the maximum monolayer loading, q_i^∞, of all components involved are of the same value[17]:

$$q_i = q_i^\infty \frac{b_i\,p_i}{1 + \sum_{i=1}^{n} b_i\,p_i} \tag{11}$$

For a non-ideal system, however, the activity coefficient must be taken into account. This extension of the IAST is also referred to as the theory of the real adsorbed solution (RAST).[15,18] It should be noted that the activity coefficients for the adsorbate phase cannot be predicted by the conventional g^E models for the liquid phase of mixtures (e.g., UNIFAC, UNIQUAC, NRTL). Therefore, the spreading pressure dependent (SPD) model introduced by Talu and Zwiebel is applied[15,19]:

$$ln\gamma_i = -s_i ln\left(\sum_{j=1}^{n} \varphi_j\,\alpha_{ij} \right) + s_i - s_i \sum_{j=1}^{n} \frac{\varphi_j\,\alpha_{ij}}{\sum_{k=1}^{n} \varphi_k\,\alpha_{jk}} \tag{12}$$

The shape factor, s_i, is calculated from the van der Waals volume of component i, $v_{w,i}$, the reference volume, v_w^0, and the lattice coordination number of the adsorbed phase, z, as follows:

$$s_i = \frac{v_{w,i}(z-2)}{v_w^0\,z} + \frac{2}{z} \tag{13}$$

The overall external contact fraction of mixture components j, φ_j, is calculated by the following:

$$\varphi_j = \frac{s_j\,x_j}{\sum_{i=1}^{n} s_i\,x_i} \tag{14}$$

The Boltzmann weighting factor, α_{ij}, satisfies the following condition:

$$\alpha_{ij} = exp\left(z \frac{e_{jj} - e_{ij}}{2\,R\,T} \right) \tag{15}$$

The average lateral interaction potential between molecules of the same species i, e_{ii}, is given as follows:

$$e_{ii} = 2 \frac{\Delta h_{ads,i}^{\pi} - \Delta h_{ads,i}^{0}}{z\,N_A\,s_i} \tag{16}$$

The cross-lateral interaction potential between components i and j of a mixture, e_{ij}, is given as follows:

$$e_{ij} = \sqrt{e_{ii}\,e_{jj}} \left(1 - \beta_{ij} \right) \tag{17}$$

where N_A denotes the Avogadro number; β_{ij} denotes the cross-lateral interaction correction parameter, which becomes zero for ideally spherical molecules; and $\Delta h_{ads,i}^{\pi}$ and $\Delta h_{ads,i}^{0}$ denote the isosteric heats of adsorption of pure component i at either the mixtures spreading pressure or zero coverage, respectively.

Another approach modified from IAST assumes a heterogeneous distribution of adsorption sites on the solid surface, which are energetically non-equivalent and occupied by the adsorbate independently of each other.[9] An equilibrium relationship according to Langmuir—also referred to as multi-site Langmuir (MSL) model—is postulated for each site independently and also solved individually applying the IAST for each site[17,20]:

$$q_i = \sum_{S=1}^{n} q_{S,i}^{\infty} \frac{b_{S,i}\,p_i}{1 + b_{S,i}\,p_i} \tag{18}$$

Assuming that the maximum monolayer loads of the components involved are the same for each site,

the multi-site multi-Langmuir (MSML) model is also valid in analogy to Equation (11):

$$q_i = \sum_{S=1}^{n} q_{S,i}^{\infty} \frac{b_{S,i}\, p_i}{1 + \sum_{i=1}^{n} b_{S,i}\, p_i} \tag{19}$$

Furthermore, the overall spreading pressure, $\tilde{\pi}$, can be expressed for both the pure component and the mixture according to Equations (20) and (21), respectively[17,21]:

$$\frac{\tilde{\pi} A}{q_i^{\infty} R T} = ln \prod_{S=1}^{n} \left(1 + b_{S,i}\, p_i^0\right) \tag{20}$$

$$\frac{\tilde{\pi} A}{q_i^{\infty} R T} = ln \prod_{S=1}^{n} \left(1 + \sum_{i=1}^{m} b_{S,i}\, p_i\right) \tag{21}$$

Coupling both equations for equal spreading pressures according to IAST yields the vapour pressure of the adsorbate phase for the single-site Langmuir (SSL):

$$p_i^0 = \frac{exp\left(\frac{\tilde{\pi} A}{q_i^{\infty} R T}\right) - 1}{b_{A,i}} \tag{22}$$

For the dual-site Langmuir (DSL) model, solving the resulting quadratic function accordingly results in the following:

$$p_i^0 = \frac{\sqrt{(b_{A,i} - b_{B,i})^2 + 4\, b_{A,i}\, b_{B,i}\, exp\left(\frac{\tilde{\pi} A}{q_i^{\infty} R T}\right)} - (b_{A,i} + b_{B,i})}{2\, b_{A,i}\, b_{B,i}} \tag{23}$$

By applying Equation (8), the activity coefficients can be estimated in an alternative way to RAST. For the SSL model, however, the resubstitution consistently yields activity coefficients of unity; only the heterogeneous MSL approaches yield deviating values.

Based on the predictive binary equilibrium data, the separation factor, which can be used as a measure of selectivity, is calculated as follows:

$$\alpha_{ij} = \frac{q_i}{y_i} \frac{y_j}{q_j} \tag{24}$$

Consequently, the selective loading capacity towards the key component, CO_2, is given by the following:

$$q_{\eta,CO_2} = q_{CO_2}\, \alpha_{CO_2,CH_4} = \frac{q_{CO_2}^2}{y_{CO_2}} \frac{y_{CH_4}}{q_{CH_4}} \tag{25}$$

2.3 | Modelling dynamic adsorption

The global mass balance for the system under consideration is calculated by coupling the component balance for the fluid (left term) and solid phase (right term) for each component i:

$$\frac{\partial c_i}{\partial t} + \frac{\partial (u\, c_i)}{\partial z} - D_{ax} \frac{\partial^2 c_i}{\partial z^2} = -\frac{1 - \varepsilon_b}{\varepsilon_b} \rho_p \frac{\partial q_i}{\partial t} \tag{26}$$

It states that the integral change of the gas phase concentration along the differential adsorber length, dz, over time, dt, which is given in the same order by an accumulation, convection, and dispersion term, must be attributed to the adsorption sink. With c_i denoting the concentration of component i, u is the advection velocity of the gas phase, D_{ax} is the axial dispersion coefficient, ρ_p is the particle density, q_i is the loading, and ε_b is the fixed beds void fraction, which is calculated from the adsorbent mass, m_{ads}, placed in the adsorber Volume, V_b:

$$\varepsilon_b = \frac{m_{ads}}{V_b\, \rho_p} \tag{27}$$

The axial dispersion coefficient is calculated as a function of Schmidt (Sc) and Reynolds (Re) number according to Wakao et al.[22,23]:

$$D_{ax} = \frac{D_{ij}}{\varepsilon_b} (20 + 0.5\, Sc\, Re) \tag{28}$$

The Chapman-Enskog free molecular diffusion coefficient is calculated as follows[24,25]:

$$D_{ij} = \frac{3}{8} \sqrt{\frac{N_A}{\pi} \frac{M_i + M_j}{2 M_i M_j}} \frac{(k_B T)^{1.5}}{p \left(\frac{\sigma_i + \sigma_j}{2}\right) \Omega_{ij}^{(2,2)}} \tag{29}$$

where N_A denotes the Avogadro constant, k_B is the Boltzmann constant, σ_i is the collision diameter, and the collision integral is calculated according to an empirical approach by Neufeld et al.[26]:

$$\Omega_{ij}^{(2,2)} = A \left(\frac{k_B T}{\varepsilon}\right)^{-B} + C\, exp\left(-D \frac{k_B T}{\varepsilon}\right) + E\, exp\left(-F \frac{k_B T}{\varepsilon}\right) \tag{30}$$

with the set of empirical parameters, $A = 1.161\,45$, $B = 0.148\,74$, $C = 0.524\,87$, $D = 0.773\,20$, $E = 2.161\,78$, and $F = 2.437\,87$ and the dispersion energy, ε. The uptake rate of the adsorbent is expressed by the linear driving force (LDF) approach by Glueckauf and Coates,[27] with the linear concentration gradient

between the loading in equilibrium to the local gas phase concentration, q_i, and the actual average adsorbent loading, $\overline{q}_i$, at the given time as the driving potential and the mass transfer coefficient, k_i, as the rate constant:

$$\frac{\partial q_i}{\partial t} = k_i (q_i - \overline{q}_i) \tag{31}$$

The mass transfer kinetics from the fluid into the porous solid is rigorously accounted for by series-connected individual transport resistances, while the process of adsorption itself is assumed to happen instantaneously and thus not to have a limiting effect. Here, the heterogeneous kinetic model postulated by Farooq and Ruthven for the interaction of micropores and macropores was modified for the system under consideration (see Equation (32))[28,29]:

$$\frac{1}{k_i} = \frac{r_p\, q_0}{3\, k_f\, c_0} + (1-\varphi_\mu)\, \frac{r_p^2\, q_0\, \tau}{15\, \varepsilon_p\, D_{K,i}\, c_0} + \varphi_\mu \frac{r_p^2}{15\, D_{\mu,i}} \tag{32}$$

The first term describes the film diffusion resistance from the bulk phase to the surface of the adsorbent particle with the radius, r_p, across the phase boundary, where q_0 corresponds to the equilibrium loading for the concentration, c_0, at feed conditions and the film diffusion coefficient, k_f, is described as a function of Sherwood number as follows[23]:

$$Sh = \frac{k_f\, d_p}{D_{ij}} = 2.0 + 1.1\, Re^{0.6}\, \sqrt[3]{Sc} \tag{33}$$

The second and third term characterize the mass transport resistance within the pore network of the particle with the tortuosity, τ, and the porosity, ε. The diffusive mass transport in the mesopores and supermicropores, which is in the range of free molecular flow for the experimental conditions with a Knudsen number $Kn >> 1$,[30] where the mean free path length of the gas molecules is significantly larger than the pore diameter, is described by the Knudsen diffusivity[31,32]:

$$D_{K,i} = \frac{d_{pore}}{3} \sqrt{\frac{8\, R\, T}{\pi\, M_i}} \tag{34}$$

In the region of ultramicropores, where the pore diameter is close to the kinetic diameter of the diffusing species, the Darken surface diffusion model[33] is used, which implies a kinetic enhancement with increasing loading for convex isotherms[34,35]:

$$D_{\mu,i} = D_{\mu,i}^{\infty} \frac{d\ln p_i}{d\ln q_i} \tag{35}$$

where the corrected Darken diffusion coefficient, $D_{\mu,i}^{\infty}$, is described by the diffusivity at standard state, $D_{\mu,i}^{0}$, via an Arrhenius type temperature dependency with the activation energy, $E_{a,i}$[36,37]:

$$D_{\mu,i}^{\infty} = D_{\mu,i}^{0}\, exp\left(-\frac{E_{a,i}}{R\, T}\right) \tag{36}$$

The terms for micro- and mesopore diffusion are weighted according to their volume fractions, determined from the pore size distributions,[9,38] with the micropore fraction, φ_μ, and the resulting mesopore fraction, $1-\varphi_\mu$.

With regard to heat transport, the heat balances for the solid (or adsorbent) phase, s, as well as for the gas phase, g, and for the wall, w, of the autoclave, a, are taken into account. The solid phase, with the release of the heat of adsorption, $\Delta h_{ads,i}$, as a result of the adsorption process, represents the heat source, $\Delta\dot{Q}_{s,ads}$, from which heat removal, takes place by means of convective, $\Delta\dot{Q}_{s,conv}$, and conductive heat transport, $\Delta\dot{Q}_{s,cond}$:

$$\Delta\dot{Q}_{s,acc} - \Delta\dot{Q}_{s,ads} + \Delta\dot{Q}_{s,conv} + \Delta\dot{Q}_{s,cond} = 0 \tag{37}$$

The accumulation term for the solid and the adsorbate phase is calculated as follows:

$$\Delta\dot{Q}_{s,acc} = \rho_p\, (1-\varepsilon_b)\, A_{cs,b}\, dz \left(\left(\sum_{n=1}^{n} M_i\, q_i c_{p,\pi,i} + c_{p,s} \right) \frac{\partial T_s}{\partial t} \right) \tag{38}$$

The heat source due to adsorptive uptake and release of adsorption enthalpy is as follows:

$$\Delta\dot{Q}_{s,ads} = \rho_p\, (1-\varepsilon_b)\, A_{cs,b}\, dz \sum_{i=1}^{n} \left(\left(\Delta h_{ads,i} - M_i\, c_{p,g,i}\, T_s \right) \frac{\partial q_i}{\partial t} \right) \tag{39}$$

The convective heat transport from solid to gas phase is as follows:

$$\Delta\dot{Q}_{s,conv} = -\alpha_p\, a_{p,v}\, (1-\varepsilon_b)\, A_{cs,b}\, dz\, (T_s - T_g) \tag{40}$$

Finally, the conductive heat transport from the solid phase to the autoclave wall according to Fourier's law is as follows:

$$\Delta\dot{Q}_{s,cond} = -\frac{2\, \lambda_s}{r_b}\, (1-\varepsilon_b)\, C_{a,in}\, dz\, (T_s - T_w) \tag{41}$$

The overall heat balance of the solid phase reads after rearrangment as follows:

$$\left(\sum_{n=1}^{n} M_i\, q_i c_{p,\pi,i} + c_{p,s}\right)\frac{\partial T_s}{\partial t} = \sum_{i=1}^{n}\left(\left(\Delta h_{ads,i} - M_i\, c_{p,g,i}\, T_s\right)\frac{\partial q_i}{\partial t}\right) - \frac{\alpha_p\, a_{p,v}}{\rho_p}\left(T_s - T_g\right) - \frac{2\,\lambda_s\, C_{a,in}}{\rho_p\, A_{cs,b}\, r_b}\left(T_s - T_w\right) \quad (42)$$

where M_i is the molar mass, ρ_p is the particle density, α_p is the convective heat transfer coefficient for the overflowed particle, $a_{p,v}$ is the volume specific particle surface, λ_s is the heat conductivity of the particle, $C_{a,in}$ is the circumference of the inner autoclave surface, $A_{cs,b}$ is the cross-sectional area of the fixed bed, r_b is the radius of the fixed bed, and $c_{p,\pi,i}$ and $c_{p,s}$ are the isobaric heat capacities of the adsorbate phase and of the solid particle, respectively.

The heat balance for the fluid phase is established accordingly:

$$\Delta\dot{Q}_{g,acc} + \Delta\dot{Q}_{s,ads} + \Delta\dot{Q}_{g,conv} - \Delta\dot{Q}_{g,disp} = 0 \quad (43)$$

With the heat accumulation in the gas phase, Equation (44) is obtained:

$$\Delta\dot{Q}_{g,acc} = c_{p,g}\,\rho_g\,\varepsilon_b\, A_{cs,b}\, dz\,\frac{\partial T_g}{\partial t} \quad (44)$$

With the heat sink due to the adsorption uptake rate from the gas phase, Equation (45) is obtained:

$$\Delta\dot{Q}_{g,ads} = -T_g\,\rho_p\,(1-\varepsilon_b)\, A_{cs,b}\, dz \sum_{i=1}^{n} c_{p,g,i}\, M_i \frac{\partial q_i}{\partial t} \quad (45)$$

With the convective heat transport from the gas phase to the solid phase, Equation (46) is obtained:

$$\Delta\dot{Q}_{g,conv} = c_{p,g}\,\varepsilon_b\, A_b\, dz\,\frac{\partial\left(u\,\rho_g\, T_g\right)}{\partial z} + \alpha_{in}\,\varepsilon_b\, C_{a,in}\, dz\left(T_g - T_w\right) + \alpha_p\, a_{p,v}\,(1-\varepsilon_b)\, A_b\, dz\left(T_g - T_s\right) \quad (46)$$

Finally, with back-mixing of heat induced due to axial dispersion, Equation (47) is obtained:

$$\Delta\dot{Q}_{g,disp} = \lambda_{ax}\,\varepsilon_b\, A_b\, dz\,\frac{\partial^2 T_g}{\partial z^2} \quad (47)$$

Rearranging the equations above again yields the overall heat balance for the gas phase:

$$c_{p,g}\,\rho_g\,\frac{\partial T_g}{\partial t} = T_g\,\rho_p\,\frac{1-\varepsilon_b}{\varepsilon_b}\sum_{i=1}^{n} c_{p,g,i}\, M_i\frac{\partial q_i}{\partial t} - c_{p,g}\frac{\partial\left(u\,\rho_g\, T_g\right)}{\partial z} - \frac{\alpha_{in}\, C_{a,in}}{A_{cs,b}}\left(T_g - T_w\right) - \frac{1-\varepsilon_b}{\varepsilon_b}\alpha_p\, a_{p,v}\left(T_g - T_s\right) + \lambda_{ax}\frac{\partial^2 T_g}{\partial z^2} \quad (48)$$

where ρ_g is the gas density, $c_{p,g}$ is the isobaric heat capacity, α_{in} is the convective heat transfer coefficient for the axial flow at the inner wall of the autoclave, $C_{a,in}$ is the circumference, and λ_{ax} is the axial heat dispersion coefficient, given by the following[22]:

$$\lambda_{ax} = \lambda_g\,(7.0 + 0.5\, Sc\, Re) \quad (49)$$

The heat balance of the autoclave wall includes the heat transport by convection and conduction:

$$\Delta\dot{Q}_{w,acc} + \Delta\dot{Q}_{w,conv} + \Delta\dot{Q}_{w,cond} = 0 \quad (50)$$

The corresponding governing equations are as follows:

$$\Delta\dot{Q}_{w,acc} = c_{p,w}\,\rho_w\, A_{cs,a}\, dz\,\frac{\partial T_w}{\partial t} \quad (51)$$

$$\Delta\dot{Q}_{w,conv} = \alpha_{in}\,\varepsilon_b\, C_{a,in}\, dz\left(T_w - T_g\right) - \alpha_{out}\, C_{a,out}\, dz\left(T_w - T_{out}\right) \quad (52)$$

$$\Delta\dot{Q}_{w,cond} = \frac{2\,\lambda_w}{s_w}\,(1-\varepsilon_b)\, C_{a,in}\, dz\,(T_w - T_s) \quad (53)$$

Reassembling of the equations finally results in following expression:

$$\mathrm{c_{p,w}}\,\rho_w\,\mathrm{A_{cs,a}}\frac{\partial \mathrm{T_w}}{\partial \mathrm{t}} = -\alpha_{in}\,\varepsilon_b\,\mathrm{C_{a,in}}\left(\mathrm{T_w} - \mathrm{T_g}\right) - \alpha_{out}\, C_{a,out}\,(T_w - T_{out}) - \frac{2\,\lambda_w}{s_w}\,(1-\varepsilon_b)\, C_{a,in}\,(T_w - T_s) \quad (54)$$

where $A_{cs,a}$ denotes the cross section of the autoclave and $c_{p,w}$ and ρ_w are its isobaric heat capacity and density, respectively. Further, α_{out} denotes the convective heat transfer coefficient for the axial flow at the outer wall of

the autoclave with the circumference, $C_{a,out}$. The ambient temperature inside the GC-oven, T_{out}, is considered as constant and equal to the feed temperature, T_f.

$$\frac{c_{p,i}}{R} = B_i + (C_i - B_i)\left(\frac{T}{A_i + T}\right)^2 \left[1 - \left(\frac{A_i}{A_i + T}\right)\left(D_i + E_i\left(\frac{T}{A_i + T}\right) + F_i\left(\frac{T}{A_i + T}\right)^2 + G_i\left(\frac{T}{A_i + T}\right)^3\right)\right] \tag{55}$$

In summary, this yields a set of $i + 3$ coupled, spatially and temporally constrained partial differential equations, which are numerically solved simultaneously for each component, i, by applying the method of finite differences in *MATLAB*, while some simplifying assumptions are made for the system under consideration. The adsorbent particles are considered as ideal isotropic spheres in a monodisperse and homogeneously distributed fixed bed fed with an ideal gas phase at Stokes flow conditions ($Re << 1$), where advective inertial forces are insignificantly small in comparison to viscous forces, in which formation of radial gradients is neglected (1D model). In addition to the convective mass and heat transport across the boundaries of the spatially discretized segments, conductive axial heat transport along both the autoclave wall and the fixed bed is taken into account. The impact of the adsorbers' periphery, which is assumed to be adiabatic, is considered up- and downstream by approximating the residence time experiments. Thereby, the delay in retention time caused by the additional pipework, and the back-mixing due to dead volumes incorporated by the armatures, are taken into account by adapting a plug flow tubular reactor (PFTR) and a continuous stirred tank reactor (CSTR) into the model setup.

The kinetic model is fitted to the experimental breakthrough data in several iteration steps. In the first step, the intracrystalline diffusion coefficient, $D^0_{\mu,i}$, and the tortuosity, τ, are determined. This procedure is performed using breakthrough curves recorded at different feed compositions ($y_{CO_2} = 0.21$ and 0.36) at $p = 5$ bar (1 bar = 10^5 Pa) and $T = 50°C$. The temperature dependent activation energy, $E_{a,i}$, is subsequently determined by temperature variation ($T = 70$ and 90°C) at $p = 5$ bar and constant feed composition ($y_{CO_2} = 0.21$). In the third step, the kinetic model is validated by pressure variation experiments ($p = 3$ bar and 7 bar) at $T = 50°C$ and $y_{CO_2} = 0.21$. In summary, this procedure yields a data set of six measured breakthrough curves per adsorbent.

The physical properties of the substances used, which could not be determined experimentally, are calculated based on corresponding literature equations. The heat capacity of the gas phase is determined according to the PPDS (physical property data services) equation[39]:

with the set of empirical parameters $A_i - G_i$ for each component, i.

Further, it is assumed that the heat capacity of the adsorbate phase, which can be assumed to be negligibly small, corresponds to that of the gas phase. The heat capacity of the resulting mixtures is estimated according to the linear mixing rule for ideal gases analogous to Dalton's law:

$$c_{p,mix} = \sum_{i=1}^{n} y_i\, c_{p,i} \tag{56}$$

The dynamic viscosity as well as the thermal conductivity of the gas phase, which are represented in the following (generalized by z_i), are calculated according to the Wassiljewa equation[40,41]:

$$z_i = A_i + B_i\, T + C_i\, T^2 + D_i\, T^3 + E_i\, T^4 \tag{57}$$

with the set of empirical parameters $A_i - E_i$ for each component, i.[39] The properties of the mixture are calculated according to Wilke as follows[42]:

$$z_{mix} = \sum_{i=1}^{n} \frac{y_i\, z_i}{y_i + \sum_{j=1}^{n-1} y_j\, \phi_{ij}} \tag{58}$$

with

$$\phi_{ij} = \frac{1}{2\sqrt{2}}\left(1 + \frac{M_i}{M_j}\right)^{-\frac{1}{2}}\left[1 + \left(\frac{z_i}{z_j}\right)^{\frac{1}{2}}\left(\frac{M_j}{M_i}\right)^{\frac{1}{4}}\right]^2 \tag{59}$$

Since the thermal conductivity of the applied adsorbents could neither be determined experimentally nor by empirical equations, the data of the structurally similar ZIF-8 are used in the context of this work according to the literature.[43]

The different heat transfer coefficients are determined according to their corresponding Nusselt number correlations (Equations (61)–(63)) as follows:

$$Nu = \frac{\alpha\, dz}{\lambda_g} \tag{60}$$

For the heat transfer coefficient between the gas phase and particles in laminar flowed through packed beds, α_p, the correlation according to Pohlhausen is applied[44]:

$$Nu = 0,664\,\sqrt{Re}\,\sqrt[3]{Pr} \tag{61}$$

where the characteristic length, L, is equivalent to the particle diameter.

The Nusselt correlation for the axially directed convective heat transfer coefficient between the gas phase and the inside of the cylinder, α_{in}, reads according to Gnielinski as follows[45]:

$$Nu = 0,664\,\sqrt{\frac{Re\, d_b}{l_b}}\,\sqrt[3]{Pr} \tag{62}$$

with L being equal to d_b.

According to Gnielinski, the Nusselt correlation for the heat transport of the cross-flown outer cylinder considers a laminar and a turbulent contribution[46]:

$$Nu = 0.3 + \sqrt{Nu_{lam}^2 + Nu_{turb}^2} \tag{63}$$

where the laminar contribution corresponds to Equation (61) and the turbulent contribution is given by the following relation:

$$Nu_{turb} = \frac{0.037\, Re^{0.8}\, Pr}{1 + 2.443\, Re^{-0.1}\left(Pr^{2/3} - 1\right)} \tag{64}$$

with L denoting the half circumference of the outer cylinder.

For the experimentally collected pure component data used in the simulations, such as the single component isotherms for the prediction of multicomponent equilibria, and the derived isosteric heats of adsorption, as well as the pore size distributions, mean diameters, and heat capacities of the used particles, the reader is referred to Part I of this study.[9]

The dimensionless quantities used for the calculations, correlations, and for the purpose of system characterization are listed in Table 1.

TABLE 1 Overview of the used dimensionless quantities

Reynolds number	$Re = \frac{\rho_g\, v\, L}{\eta_g}$
Schmidt number	$Sc = \frac{\eta_g}{D_{ij}\,\rho_g}$
Peclet number (mass)	$Pe' = \frac{d_p\, v}{D_{ij}} = Re\, Sc$
Bodenstein number	$Bo = \frac{v\, L}{D_{ax}}$
Knudsen number	$Kn = \frac{\lambda}{d_{pore}}$
Biot number	$Bi = \frac{\alpha\, L}{\lambda_s}$
Prandtl number	$Pr = \frac{\eta_g\, c_{p,g}}{\lambda_g}$
Peclet number (heat)	$Pe = \frac{L\, v\, \rho\, c_p}{\lambda} = Re\, Pr$

The pressure drop over the packed bed is calculated by solving the momentum balance according to Ergun's equation[47]:

$$\Delta p = \frac{150\,\eta_g\, l_b}{d_p^2}\,\frac{(1-\varepsilon_b)^2}{\varepsilon_b^3}\,u_s + \frac{1.75\, l_b\, \rho_g}{d_p}\,\frac{(1-\varepsilon_b)}{\varepsilon_b^3}\,u_s^2 \tag{65}$$

where u_s denotes the superficial gas velocity.

3 | RESULTS AND DISCUSSION

The adsorption phase equilibria predicted by the previously presented models for the binary mixture of CO_2 and CH_4 are shown in Figure 2 (and Figure S1 of the Supporting Information [SI], respectively) for all IFPs at a system pressure of 5 bar and a temperature of 50°C. The various models do not show major deviations from each other for the respective IFPs and are in good agreement to the experimental data, which are obtained by integration of the breakthrough curves (see Section 2.1) of binary CO_2/CH_4-mixtures at feed compositions of $y_{CO_2} = 0.21$ and 0.36, respectively (see Section 2.3 and Table 2). However, relatively large deviations are found for the equilibrium loading of methane for IFP-2 to -5. This matter will be addressed in more detail later during the kinetic considerations. The largest deviations among the models are partly seen for the ML-DSL/ML-EL (dashed lines) and the IAST-DSL (yellow line) approaches. The latter is reflected in the non-ideal behaviour of the derived activity coefficients (see Figure 3). However, the RAST calculation (red line) does not seem to deviate much from the ideal behaviour and is very close to the IAST-EL data (blue line), resulting in activity coefficients of unity. Therefore, the RAST approach is not considered for further dynamic simulations. In order to simulate non-isothermal and pressure-dependent

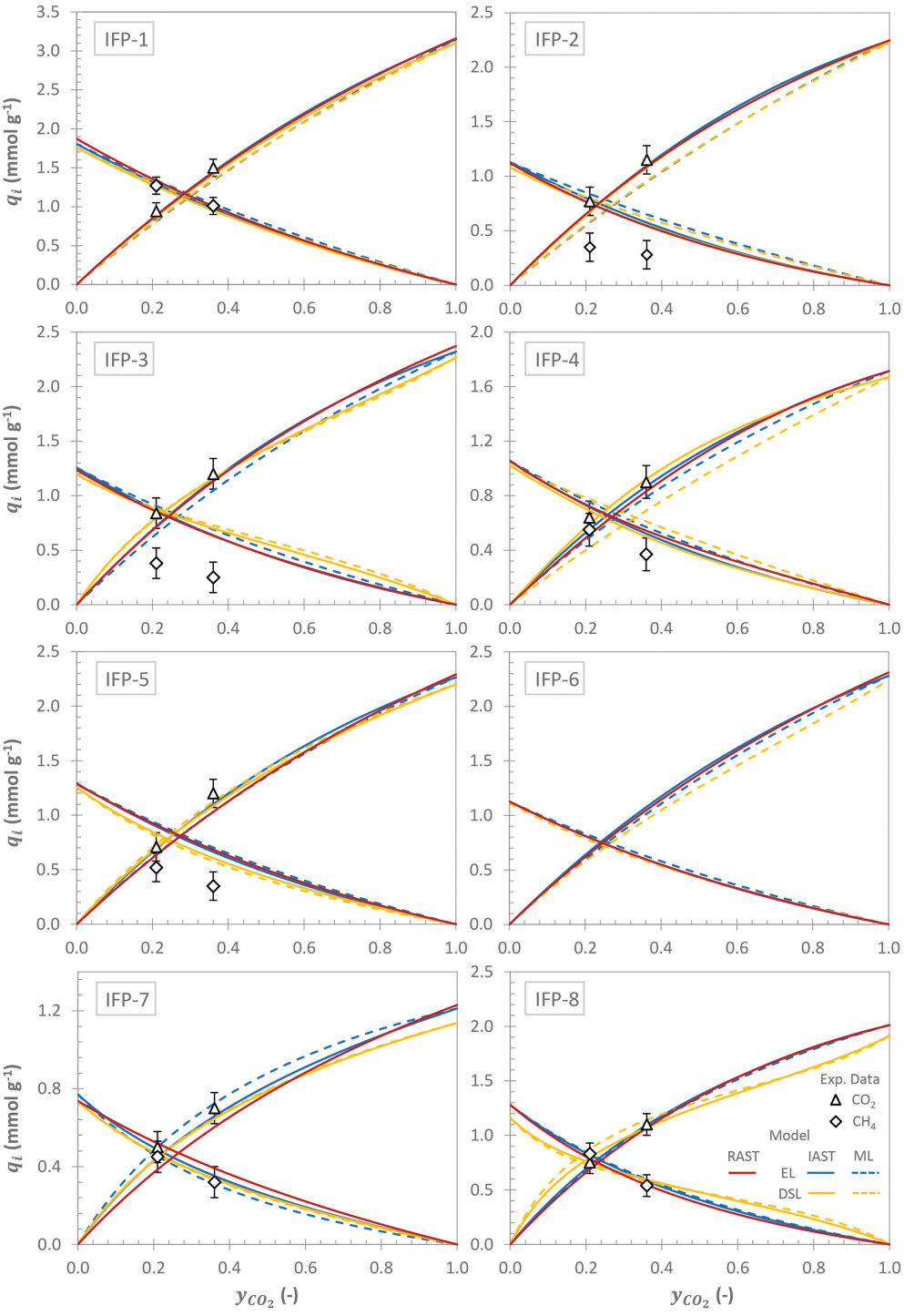

FIGURE 2 Binary adsorption equilibria of CO_2 and CH_4 on all imidazolate framework Potsdam (IFP) samples at $p = 5$ bar and $T = 323.15$ K. Comparison of predictive models (modified Langmuir [ML], ideal adsorbed solution theory [IAST], real adsorbed solution theory [RAST]) based on pure component isotherm data ($V_{occ} = V_{ads}$) to experimental data obtained from integration of breakthrough curves with mixture compositions of $y_{CO_2} = 0.21$ and 0.36, respectively

TABLE 2 Overview of the design of experiments (DoE) for dynamic adsorption of binary CO_2/CH_4-mixtures on the imidazolate framework Potsdam (IFP) samples in a fixed bed

Varied quantity	Static quantities	Experiment 1	Experiment 2
y_{CO_2}	$T = 50°C$ $p = 5$ bar	$y_{CO_2} = 0.21$	$y_{CO_2} = 0.36$
T	$y_{CO_2} = 0.21$ $p = 5$ bar	$T = 70°C$	$T = 90°C$
p	$y_{CO_2} = 0.21$ $T = 50°C$	$p = 3$ bar	$p = 7$ bar

Note: 1 bar = 10^5 Pa.

dynamic adsorption, the binary equilibria are extended to the relevant temperature and pressure range in addition to the concentration dependence. The resulting three-dimensional solution domains are visualized by means of the separation factor and the selective loading capacity in the SI section (Figures S2–S17).

It follows from the figures that, in general, for all IFPs the EL-based separation factor (Figures S2 and S3) increases with increasing CO_2 concentration in the gas mixture and with decreasing temperature, respectively. Only IFP-7 shows the opposite behaviour, whereas for IFP-8 the separation factor shows a minimum at approximately 345 K with increasing effectiveness for high CO_2 concentrations at higher temperatures and vice versa with decreasing effectiveness. The DSL-based (Figures S3 and S4) separation factors in several cases show local extrema and exhibit a more complex behaviour. IFP-2, with a maximum of 10, shows on average the highest

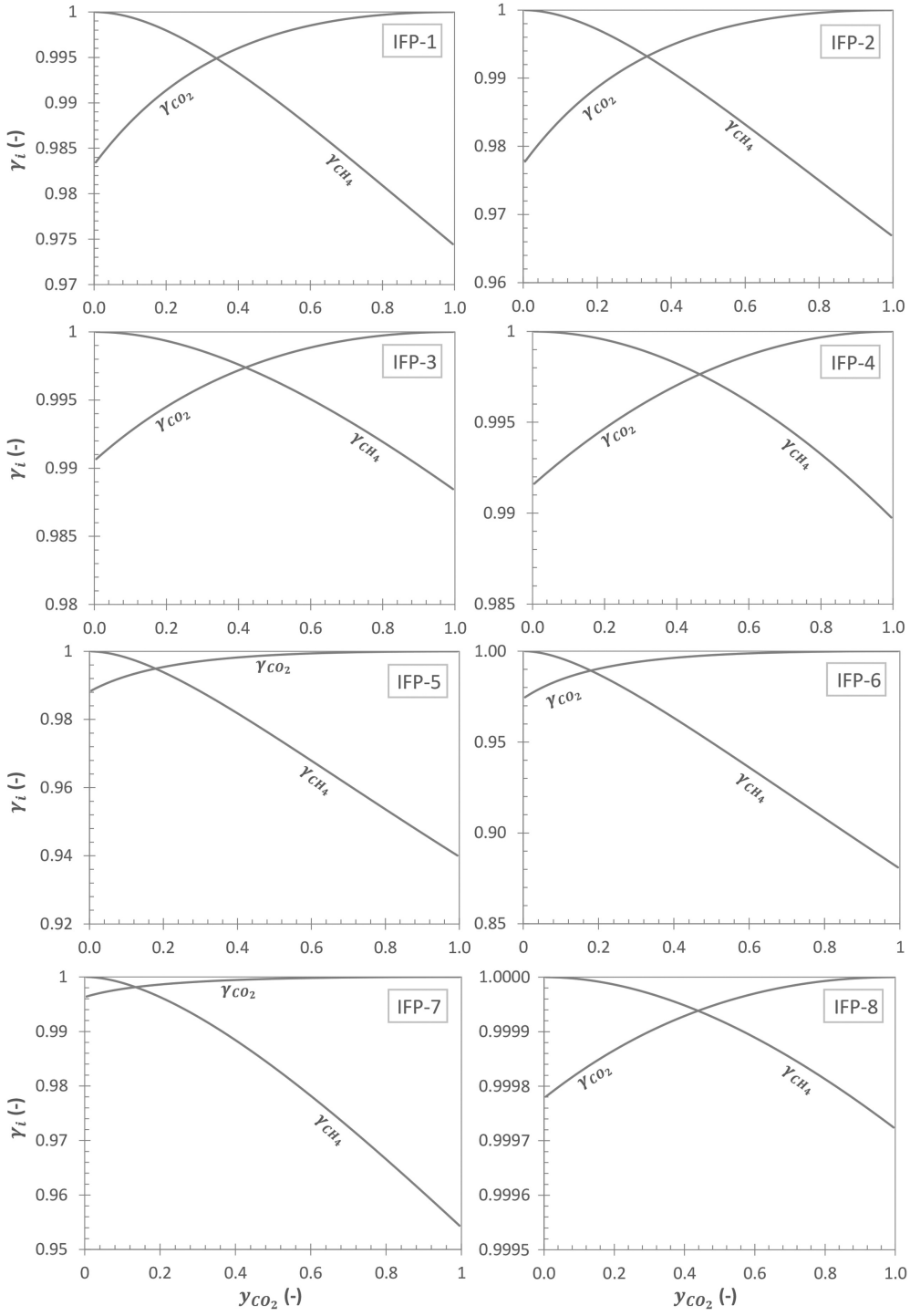

FIGURE 3 Activity coefficients for the binary CO_2/CH_4 mixture at $p = 5$ bar and $T = 323.15$ K derived from the dual-site Langmuir—Ideal adsorbed solution theory (DSL-IAST) approach

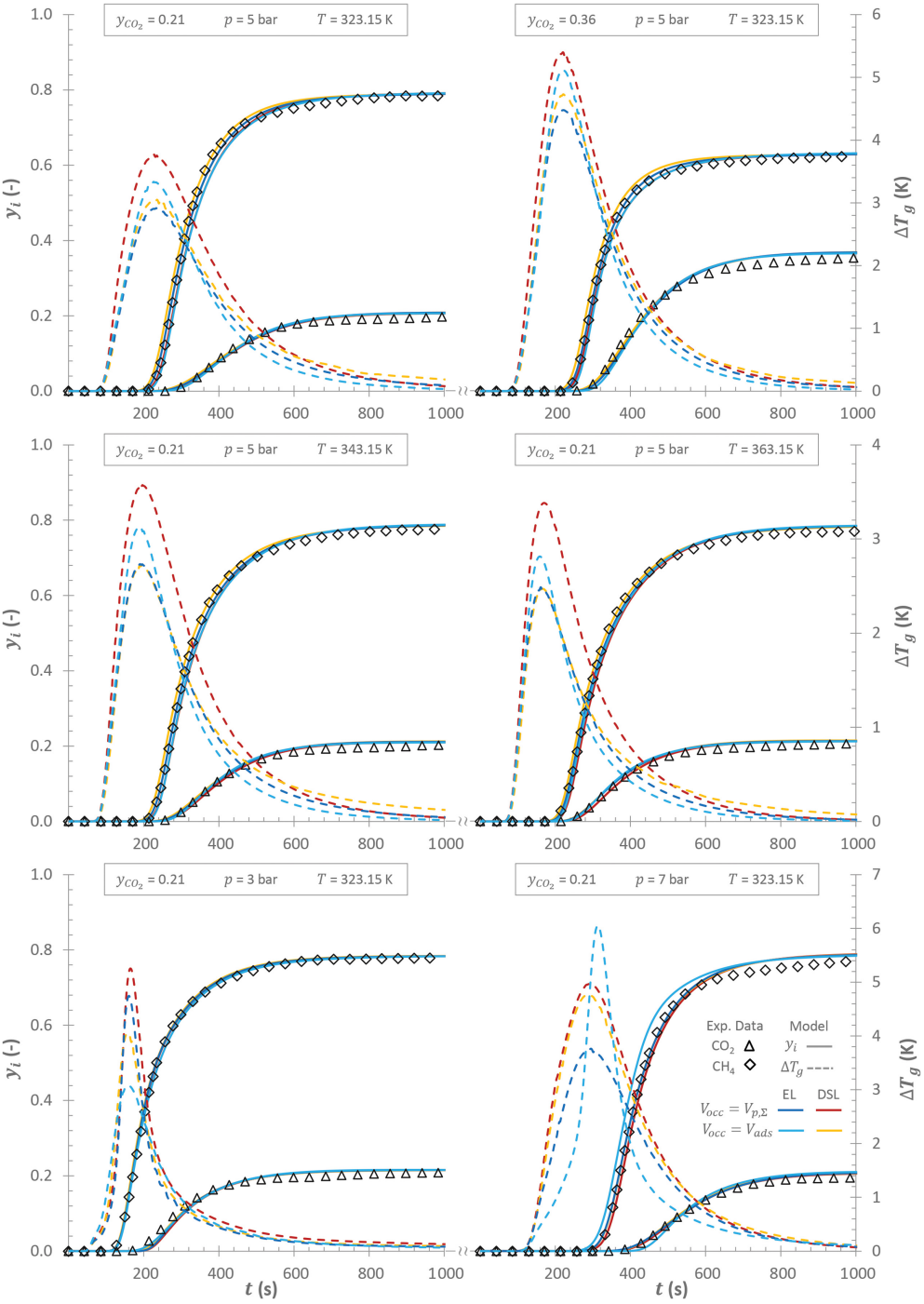

FIGURE 4 Comparison of the experimental breakthrough data of binary CO_2/CH_4-mixtures on IFP-1 according to the design of experiments (DoE) chart (Table 2) to the simulated concentration (y_i, primary axis) and temperature (ΔT_g, secondary axis) profiles. Note that the inner axes of two adjacent plots are hidden due to space limitations

separation factors, and IFP-7, with a maximum of 4, the lowest, which is in good agreement with the previous findings.[9] However, no significant differences can be observed here for IFP-1 or for the remaining IFPs, which all range around the same values. The selective loading capacities show good agreement to the trends of the pure substance data,[9] with the best values again for IFP-2 with up to 40, followed by IFP-1, and the worst values for IFP-7, with a maximum of 5.

With regard to variable pressure (Figures S10–S17) the IFPs show similar trends as described in the previous observations, exhibiting the highest separation factors at high pressure and low temperature according to Le Chatelier's principle of the least constraint but with the same remarkable anomalies for IFP-7 and -8.

In order to obtain detailed information about the adsorption kinetics, the measurement of the breakthrough curves is based on the experimental strategy according to Table 2 as described in Section 2.3.

For the sake of clarity, only the experimental breakthrough data of IFP-1 are shown within the text (see Figure 4) together with the simulation results of the

concentration and temperature profiles for all four presented IAST-based mixture adsorption models (IAST-EL, IAST-DSL, each with both types of buoyancy corrections: $V_{occ} = V_{\pi}$, $V_{occ} = V_{p,\Sigma}$) as representative of all IFPs. The breakthrough data for the remaining IFPs can be found in the SI (Figure S18–S23; note: For IFP-6, no data could be collected because the available quantities were insufficient). For IFP-1, the simulations agree almost identically with the experimental data—also at different conditions—for each mixture adsorption model, with the smallest deviations for IAST-EL ($V_{occ} = V_{p,\Sigma}$). This observation, in addition to the integral solution (see Figure 2), validates once again the predictive equilibrium approach according to IAST. With IFP-2 (Figure S18) however, underestimations of the CO_2 loading occur, which are especially significant for the temperature and pressure variations, resulting in decreased retention times for CO_2 compared to the experimental data.

The best approximation for IFP-2 is provided by the IAST-EL approaches. For IFP-3, -4, and -5 (see Figures S19–S21) there are also slight CO_2 underestimations recognizable with IAST-DSL ($V_{occ} = V_{\pi}$), IAST-DSL ($V_{occ} = V_{p,\Sigma}$), and IAST-DSL ($V_{occ} = V_{p,\Sigma}$) as the best approaches, respectively. The largest differences between the equilibrium models applied can be seen for IFP-7 and -8. For both adsorbents, the EL approach fits the data better, especially at elevated pressures. Nevertheless, each of the applied models can be used with good correspondence.

However, in order to understand transient processes in detail, a kinetic analysis is indispensable. Table 3 shows the approximated kinetic model parameters corresponding to the individual systems under investigation, which were determined according to the procedure described in Section 2.3. It is apparent that the intracrystalline diffusion coefficients for CO_2 are all, without exception, larger than for CH_4. This trend as well as the order of magnitude of the diffusivities, with values ranging from 10^{-9} to 10^{-13}, is in good agreement with reported data for structurally similar MOF species, such as the zinc-based ZIF-8[48] and the cobalt-based ZIF-9.[49] The generally larger diffusion resistance of CH_4 can be explained by its larger kinetic diameter ($d_{k,CH_4} = 3.8$ Å; 1 Å = 0.1 nm) compared to CO_2 ($d_{k,CO_2} = 3.3$ Å).

The tortuosities, with values around 3, are also in good agreement with literature data.[50,51] Having a closer look at the adsorbent-specific diffusivities reveals, that especially for IFP-2, -3, -4, and -5, CH_4-diffusivities are within two to four orders of magnitude lower than CO_2-diffusivities, while the differences for IFP-1, -7, and -8 are significantly smaller. An explanation for the strong preference of CO_2 could be polar effects of the halogenated IFP-2 and -3 and the Co-based IFP-5, as well as the gate opening effect of the ethyl group of IFP-4. The kinetic effects become even more obvious when plotting the overall mass transfer resistances for both components versus time (see Figure 5), which are calculated by the heterogeneous kinetic model according to Equation (32). As the kinetics are in most cases exclusively limited by micropore diffusion; the contributions of film and mesopore diffusion remain insignificant in the following considerations.

In view of the different diffusion coefficients for IFP-2 and -3 as well as for IFP-4 and -5, one might wonder why both pairs nevertheless exhibit similarly large mass transfer resistances. This phenomenon is primarily to be attributed to the different particle radii.[9,38] Additionally, in the case of IFP-3, the isotherm slope occurs to be extremely flat in comparison,[9] which further amplifies the mass transport resistance according to the Darken equation (Equation (32)). In order to shed more light on whether the separation is kinetic- or equilibrium-driven, the respective saturation curves of the adsorbents are shown comparatively for CO_2 and CH_4 in Figure 6, where the saturation reflects the ratio of actual loading to equilibrium loading. For IFP-1, saturation loadings are reached very quickly for both CO_2 and CH_4, with

TABLE 3 Estimated intracrystalline diffusion coefficients, $D^0_{\mu,i}$, activation energies, $E_{a,i}$, and tortuosities, τ, by approximation of the kinetic model to the experimental data

Species	D^0_{μ,CO_2} ($m^2\ s^{-1}$)	D^0_{μ,CH_4} ($m^2\ s^{-1}$)	E_{a,CO_2} (kJ mol^{-1})	E_{a,CH_4} (kJ mol^{-1})	τ (−)
IFP-1	$3.99 \cdot 10^{-10}$	$1.08 \cdot 10^{-10}$	13.73	14.84	2.96
IFP-2	$1.70 \cdot 10^{-9}$	$3.66 \cdot 10^{-13}$	13.35	12.85	3.30
IFP-3	$5.18 \cdot 10^{-9}$	$9.18 \cdot 10^{-13}$	14.31	9.89	3.07
IFP-4	$1.38 \cdot 10^{-9}$	$3.03 \cdot 10^{-11}$	13.35	12.85	3.30
IFP-5	$2.14 \cdot 10^{-10}$	$5.52 \cdot 10^{-12}$	16.43	13.36	2.53
IFP-7	$2.67 \cdot 10^{-10}$	$5.19 \cdot 10^{-11}$	15.51	14.38	3.11
IFP-8	$6.05 \cdot 10^{-11}$	$1.47 \cdot 10^{-11}$	14.51	8.34	3.17

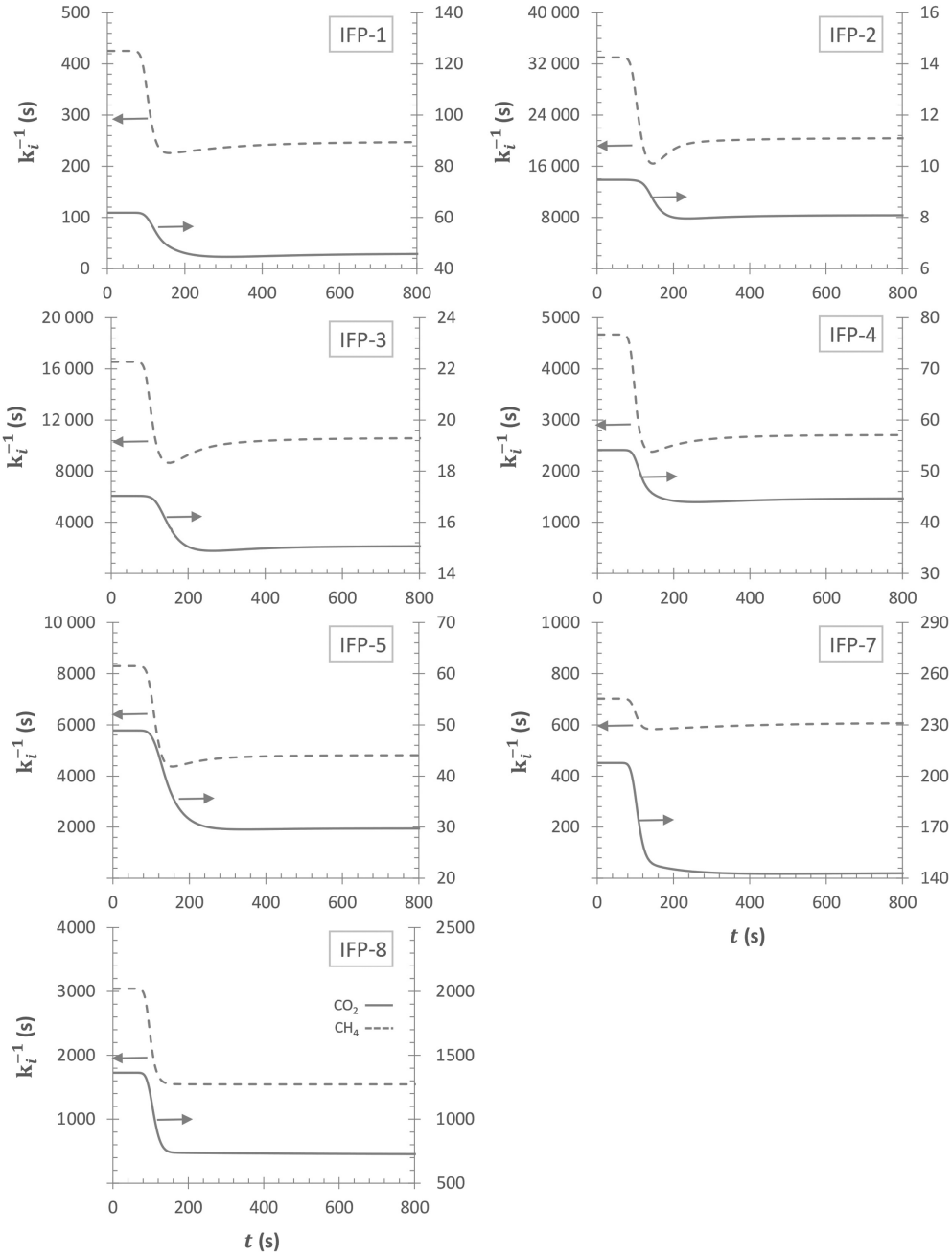

FIGURE 5 Overall mass transport resistance during the dynamic mixed gas adsorption of CO_2 (straight line) and CH_4 (dashed line) in a fixed bed for each imidazolate framework Potsdam (IFP) sample (experiment 1/concentration variation, see Table 2) according to the heterogeneous kinetic model (see Equation (32))

equilibration times, t_{eq}, of 500 and 1000 s, respectively, which are both in the range of the transient breakthrough regime, where significant separation takes place. In this case, the adsorption process is not kinetically limited and thus is solely equilibrium driven. For IFP-2 to -5, however, equilibrium for CH_4 is reached extremely slowly ($t_{eq,CH_4} >> 1000$ s), while CO_2 equilibrates immediately ($t_{eq,CO_2} < 1000$ s), which has a favourable effect on the separation efficiency by kinetically selecting the faster diffusing CO_2. The extremely long equilibration times also caused the negative deviations of the equilibrium loadings for CH_4 derived from integration of the concentration profiles of the respective samples (see Figure 2). Although IFP-7 shows a similar kinetic-selective behaviour as IFP-2 to -5, no significant separation can be observed, which in this case can be attributed to the low separation factors (Figures S2–S5) and selective loading capacities (Figures S6–S9). IFP-7 is also kinetically limited with regards to CH_4 ($t_{eq,CH_4} >> 1000$ s). IFP-8 shows not only a kinetic limitation for CH_4 but also for CO_2, which in turn also results in a loss of separation efficiency.

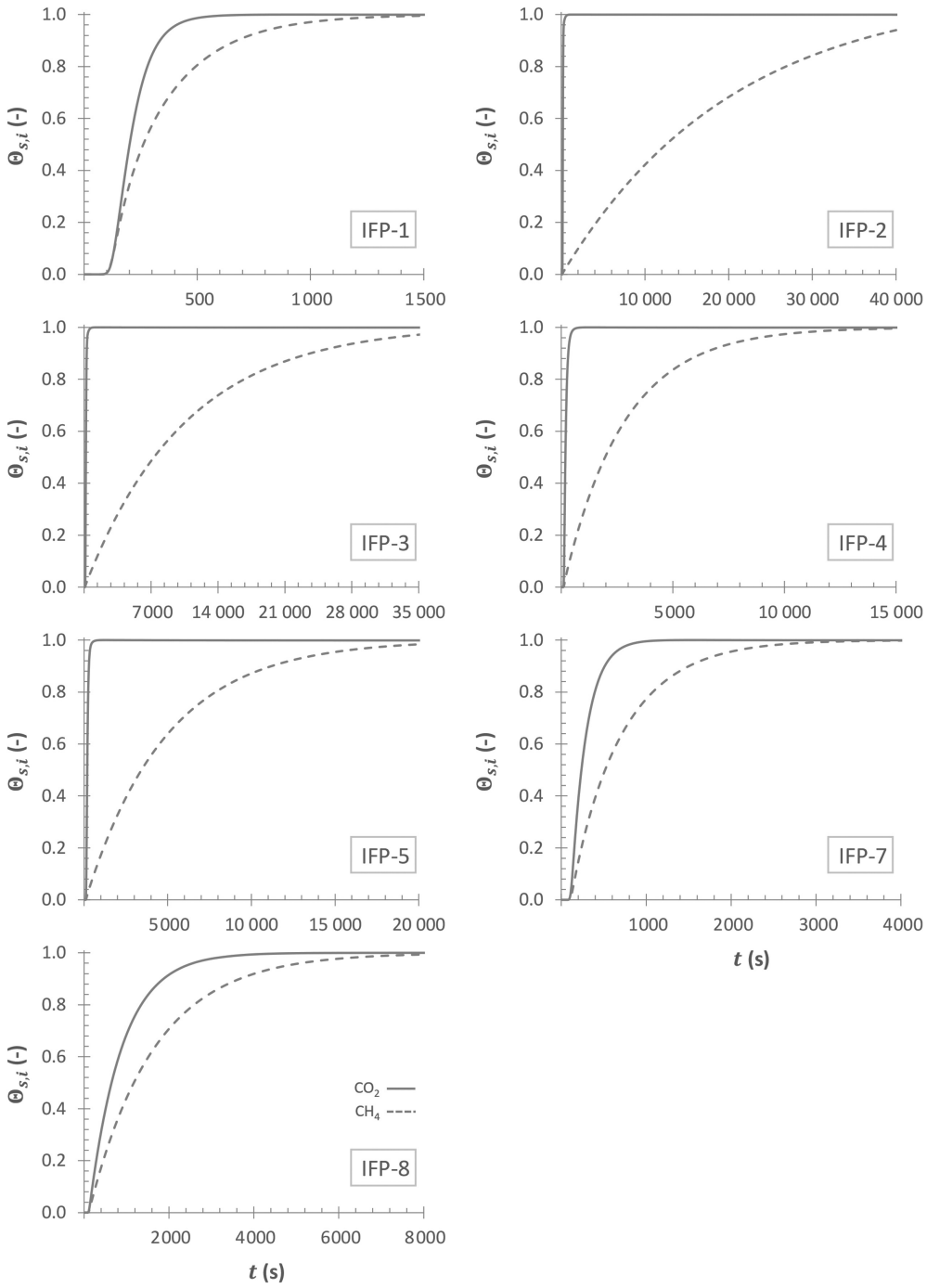

FIGURE 6 Mass transport limited saturation behaviour during the dynamic mixed gas adsorption of CO_2 (straight line) and CH_4 (dashed line) in a fixed bed for each imidazolate framework Potsdam (IFP) sample (experiment 1/concentration variation, see Table 2)

4 | CONCLUSIONS

A model for the non-isothermal simulation of dynamic adsorption of binary CO_2/CH_4-mixtures in a fixed bed column was presented and validated on the basis of experimental data. The adsorbents used were the isoreticular series of microporous IFPs (IFP-1 to -8), whose material characteristic were already reported in Part I of this study.[9] For the model calculations, both mass and energy balances were considered, resulting in a system of coupled partial differential equations. Different predictive models for the description of mixture adsorption based on pure component isotherm data were compared and evaluated. It could be shown that all approaches (RAST and IAST as well as ML for EL and DSL isotherm models) generally show no significant differences between each other, which is an indicator for ideal behaviour. This was additionally confirmed by the good agreement of the simulation results to experimental breakthrough data for all IFPs at different feed concentrations, temperatures, and pressures. The only significant deviations are shown for IFP-2 at elevated pressures

and temperatures. Also, the different approaches regarding the consideration of the displaced sample volume in the buoyancy correction—adsorbate volume ($V_{occ} = V_{\pi}$) versus total pore volume ($V_{occ} = V_{p,\Sigma}$)—for the calculation of the absolute loading from gravimetric experiments[9] show no major differences in the simulation results. A detailed study of the heterogeneous adsorption kinetic model provided the information that, for IFP-1 alone, the adsorption process is not mass transport limited and is thus equilibrium-driven. IFP-2, -3, -4, -5, and -7 exhibit comparatively extremely high mass transfer resistances for CH_4, resulting in slow CH_4 saturation of the adsorbent, while equilibrium is reached almost instantaneously for CO_2. The kinetic selectivity towards CO_2 in addition to the equilibrium selectivity results in a desirable enhancement of the separation efficiency. However, the loading capacity for IFP-7 is so low that even the kinetically induced increase in selectivity does not result in significant separation of the components. For IFP-8, in addition to CH_4, CO_2 mass transport is also strongly limited. In this case, the separation efficiency also decreases, since the saturation loadings of both components are only reached gradually within breakthrough time. The comparison of the equilibrium data (calculated by integrating the concentration profiles) with the predictive approaches showing negative deviations for CH_4 for the extremely diffusion-limited IFP-2 to -5 (see Figure 2), confirms this statement. The estimated intracrystalline diffusion coefficients for micropore diffusion are in good accordance with literature data for the similarly structured ZIF-MOFs.

PEER REVIEW

The peer review history for this article is available at https://publons.com/publon/10.1002/cjce.24288.

NOMENCLATURE

Latin symbols

a	specific surface/lower integration limit ($m^2\ g^{-1}$/-)
$\widetilde{a}$	volume specific surface (m^{-1})
A	interface between gas and adsorbate phase/area (m^2)
b	affinity constant/upper integration limit (Pa^{-1}/-)
Bi	Biot number (-)
Bo	Bodenstein number (-)
c	concentration (mol m^{-3})
c_p	specific isobaric heat capacity (J g^{-1} K^{-1})
C	circumference (m^2)
d	diameter (m)
D_{ax}	axial dispersion coefficient ($m^2\ s^{-1}$)
D_{ij}	molecular diffusion coefficient ($m^2\ s^{-1}$)
D_K	Knudsen diffusion coefficient ($m^2\ s^{-1}$)
D_{μ}	intracrystalline diffusion coefficient ($m^2\ s^{-1}$)
E_a	activation energy (J mol^{-1})
Δh_{ads}	heat of adsorption (J mol^{-1})
f	function (-)
g	molar Gibbs free energy (J mol^{-1})
k	rate constant (s^{-1})
k_0	equilibrium constant at reference state (-)
k_B	Boltzmann constant (-)
k_f	film diffusion rate consant (m s^{-1})
Kn	Knudsen number (-)
l	length (m)
m	mass (g)
M	molar mass (g mol^{-1})
n	number of moles/isotherm parameter (Sips model) (mol/-)
N_A	Avogadro number (-)
Nu	Nusselt number (-)
p	pressure (Pa)
p^{sat}	saturation vapour pressure (Pa)
Pe	Peclet number heat (-)
Pe'	Peclet number mass (-)
Pr	Prandtl number (-)
q	loading (mol g^{-1})
q^{∞}	maximum loading (monolayer) (mol g^{-1})
$\overline{q}$	actual average loading (mol g^{-1})
q_{η}	selective loading capacity (mol g^{-1})
$\Delta\dot{Q}$	heat transfer rate (W)
r	radius (m)
R	universal gas constant (J mol^{-1} K^{-1})
Re	Reynolds number (-)
s	molar entropy/shape factor (J mol^{-1} K^{-1}/-)
S	selectivity (-)
Sc	Schmidt number (-)
T	absolute temperature (K)
t	time (s)
u	advection velocity (m s^{-1})
u_s	superficial velocity (m s^{-1})
v	molar volume ($m^3\ mol^{-1}$)
$v_{w,i}$	van der Waals volume ($m^3\ mol^{-1}$)
v_w^0	van der Waals reference volume ($m^3\ mol^{-1}$)
V	volume (m^3)
$\dot{V}$	volumetric flow rate ($m^3\ s^{-1}$)
x	variable/liquid phase mole fraction (-/-)
y	gas phase mole fraction (-)
z	lattice coordination number/length vector (-/m)

Greek symbols

α	convective heat transfer coefficient (W m^{-2} K^{-1})
α_{ij}	Boltzmann weighting factor/separation factor (-/-)
β_{ij}	cross-lateral interaction correction parameter (-)
γ	activity coefficient (-)
Δ	uncertainty (-)

ε	void fraction (-)
η	dynamic viscosity (Pa s)
ϑ	relative temperature (°C)
λ	heat conductivity (W m^{-1} K^{-1})
λ_{ax}	axial heat dispersion coefficient (W m^{-1} K^{-1})
π	spreading pressure (N m^{-1})
$\widetilde{\pi}$	overall spreading pressure (N m^{-1})
ρ	density (g m^{-3})
σ	collision diameter (m)
Σ	void fraction (-)
τ	tortuosity (-)
φ	overall external contact fraction (-)
φ_μ	micropore fraction (-)
ψ	pore size distribution (-)
χ	electronegativity on the Pauling scale (-)
$\Omega_{ij}^{(2,2)}$	collision integral (-)

Subscripts

a	autoclave
acc	accumulation
ads	adsorption
b	bed
conv	convection
cond	conduction
CS	cross section
f	feed
g	gas phase
i	component i
in	inner wall side
j	component j
lam	laminar
m	material
μ	micro
mix	mixture
occ	occupied
out	outer wall side
p	particle
pore	pore
π	adsorbate phase
s	solid
S	site number
STP	standard temperature and pressure
Σ	sum
t	total
turb	turbulent
w	wall

Superscripts

0	reference state
abs	absolute
π	adsorbate phase
g	gas phase
∞	infinity/maximum

Abbreviations

A	adsorber column
B	bubbler
CSTR	continuous stirred tank reactor
CH_4	methane
Co	cobalt
CO_2	carbon dioxide
DSL	dual site Langmuir
EL	extended Langmuir
GC	gas chromatography
H_2O	water
H_2S	hydrogen sulphide
IFP	imidazolate framework Potsdam
IAST	ideal adsorbed solution theory
LDF	linear driving force
MFC	mass flow controller
MFM	mass flow meter
ML	multi-Langmuir
MOF	metal organic framework
MS	mass spectrometer
MSL	multi-site Langmiur
N_2	nitrogen
NG	natural gas
PFTR	plug flow tubular reactor
PPDS	physical property data services
RCV	remotely controlled valve
RAST	real adsorbed solution theory
SPD	spreading pressure dependent
SSL	single site Langmuir
ZIF	zeolitic imidazolate framework
Zn	zinc

REFERENCES

[1] B. Looney, *Statisitical Review of World Energy*, 69th ed., London, UK **2020**.

[2] R. W. Baker, K. Lokhandwala, *Ind. Eng. Chem. Res.* **2008**, *47*, 2109.

[3] C. Chen, D. Zheng, G.-J. Liu, L.-W. Deng, Y. Long, Z.-H. Fan, *Waste Manage.* **2015**, *38*, 436.

[4] R. Mulka, W. Szulczewski, J. Szlachta, H. Prask, *Clean Technol. Envir.* **2016**, *18*, 807.

[5] M. B. Kermani, A. Morshed, *Corrosion* **2003**, *59*, 659.

[6] B. Mishra, S. Al-Hassan, D. L. Olson, M. M. Salama, *Corrosion* **1997**, *53*, 852.

[7] R. H. Hugman, E. H. Vidas, P. S. Springer, *Chemical Composition of Discovered and Undiscovered Natural Gas in the Lower-48 United States* (PB-91-144600/XAB; CNN: GRI-5088-222-1745), **1990**, https://www.osti.gov/biblio/6087223-chemical-composition-discovered-undiscovered-natural-gas-lower-united-states-project-summary-final-report-november-march (accessed: April 2021).

[8] M. Miltner, A. Makaruk, M. Harasek, *J. Clean. Prod.* **2017**, *161*, 1329.

[9] D. Otter, M. Dieler, V. Dänekas, L. Krätz, H.-J. Holdt, H.-J. Bart, *Can. J. Chem. Eng.* **2021**. https://doi.org/10.1002/cjce.24286.

[10] W. Kwapinski, K. Salem, D. Mewes, E. Tsotsas, *Chem. Eng. Sci.* **2010**, *65*, 4250.
[11] D. Otter, S.-J. Ernst, L. Krätz, H.-J. Bart, *SN Applied Sciences* **2020**, *2*, 4899.
[12] L. Dedić, M. Matić, J. Pečarić, *ANZIAM J.* **2005**, *46*, 417.
[13] A. L. Myers, J. M. Prausnitz, *AIChE J.* **1965**, *11*, 121.
[14] S. Brandani, E. Mangano, L. Sarkisov, *Adsorption* **2016**, *22*, 261.
[15] O. Talu, I. Zwiebel, *AIChE J.* **1986**, *32*, 1263.
[16] E. C. Markham, A. F. Benton, *J. Am. Chem. Soc.* **1931**, *53*, 497.
[17] A. L. Myers, *AIChE J.* **1983**, *29*, 691.
[18] E. Costa, J. L. Sotelo, G. Calleja, C. Marrón, *AIChE J.* **1981**, *27*, 5.
[19] A. Ladshaw, S. Yiacoumi, C. Tsouris, *AIChE J.* **2015**, *61*, 2600.
[20] T. Nitta, T. Shigetomi, M. Kuro-Oka, T. Katayama, *J. Chem. Eng. Jpn.* **1984**, *17*, 39.
[21] C. Minka, A. L. Myers, *AIChE J.* **1973**, *19*, 453.
[22] N. Wakao, T. Funazkri, *Chem. Eng. Sci.* **1978**, *33*, 1375.
[23] E. Tsotsas, E.-U. Schlünder, *Heat Mass Transfer* **1990**, *25*, 245.
[24] D. Enskog, *Arkiv för Matematik, Astronomi och Fysik* **1921**, *16*, 60.
[25] S. Chapman, *Philos. T. R. Soc. Lond.* **1918**, *217*, 115.
[26] P. D. Neufeld, A. R. Janzen, R. A. Aziz, *J. Chem. Phys.* **1972**, *57*, 1100.
[27] E. Glueckauf, J. I. Coates, *J. Chem. Soc.* **1947**, 1315.
[28] S. Farooq, D. M. Ruthven, *Ind. Eng. Chem. Res.* **1990**, *29*, 1084.
[29] S. Farooq, D. M. Ruthven, *Ind. Eng. Chem. Res.* **1990**, *29*, 1076.
[30] R. Villet, R. Wilhelm, *Ind. Eng. Chem.* **1961**, *53*, 837.
[31] D. M. Ruthven, W. J. DeSisto, S. Higgins, *Chem. Eng. Sci.* **2009**, *64*, 3201.
[32] N. Nishiyama, *J. Membrane Sci.* **2001**, *182*, 235.
[33] L. S. Darken, *Transactions of the AIME* **1948**, *175*, 184.
[34] D. D. Do, H. D. Do, *Adsorption* **2001**, *7*, 189.
[35] Y. D. Chen, R. T. Yang, *AIChE J.* **1991**, *37*, 1579.
[36] A. I. Skoulidas, D. S. Sholl, *J. Phys. Chem. B* **2001**, *105*, 3151.
[37] M. Khalighi, S. Farooq, I. A. Karimi, *Ind. Eng. Chem. Res.* **2012**, *51*, 10659.
[38] D. Otter, S. S. Mondal, A. Alrefai, L. Krätz, H.-J. Holdt, H.-J. Bart, *Nanomaterials* **2021**, *11*, 1400.
[39] *VDI-Wärmeatlas* (Ed: VDI-Gesellschaft Verfahrenstechnik und Chemieingenieurwesen), 11th ed., Springer, Berlin, Germany **2013**.
[40] A. Wassiljewa, *Phys. Z.* **1904**, *5*, 737.
[41] M. P. Saksena, S. C. Saxena, *Appl. Sci. Res.* **1967**, *17*, 326.
[42] C. R. Wilke, *J. Chem. Phys.* **1950**, *18*, 517.
[43] B. Cui, C. O. Audu, Y. Liao, S. T. Nguyen, O. K. Farha, J. T. Hupp, M. Grayson, *ACS Appl. Mater. Inter.* **2017**, *9*, 28139.
[44] E. Pohlhausen, *Z. Angew. Math. Mech.* **1921**, *1*, 115.
[45] V. Gnielinski, *Verfahrenstechnik* **1978**, *12*, 363.
[46] V. Gnielinski, *Forsch. Ingenieurwes.* **1975**, *41*, 145.
[47] S. Ergun, *Chem. Eng. Prog.* **1952**, *48*, 89.
[48] A.-K. Pusch, T. Splith, L. Moschkowitz, S. Karmakar, R. Biniwale, M. Sant, G. B. Suffritti, P. Demontis, J. Cravillon, E. Pantatosaki, F. Stallmach, *Adsorption* **2012**, *18*, 359.
[49] J. Liu, C. Liu, A. Huang, *Int. J. Hydrogen Energ.* **2020**, *45*, 703.
[50] B. Ghanbarian, A. G. Hunt, R. P. Ewing, M. Sahimi, *Soil Sci. Soc. Am. J.* **2013**, *77*, 1461.
[51] X. Hu, S. Brandani, A. I. Benin, R. R. Willis, *Ind. Eng. Chem. Res.* **2015**, *54*, 5777.

SUPPORTING INFORMATION

Additional supporting information may be found in the online version of the article at the publisher's website.

How to cite this article: D. Otter, M. Dieler, V. Dänekas, C. Geitner, L. Krätz, H.-J. Holdt, H.-J. Bart, *Can. J. Chem. Eng.* **2022**, *100*(8), 1902. https://doi.org/10.1002/cjce.24288